IEEE TRANSACTIONS ON

GEOSCIENCE AND REMOTE SENSING

A PUBLICATION OF THE IEEE GEOSCIENCE AND REMOTE SENSING SOCIETY

NOVEMBER 2008 VOLUME 46 NUMBER 11 IGRSD2 (ISSN 0196-2892)

PART I OF TWO PARTS

SPECIAL SECTION ON METEOROLOGY, CLIMATE, IONOSPHERE, GEODESY, AND REFLECTIONS FROM THE OCEAN SURFACES: STUDIES BY RADIO OCCULTATION METHODS

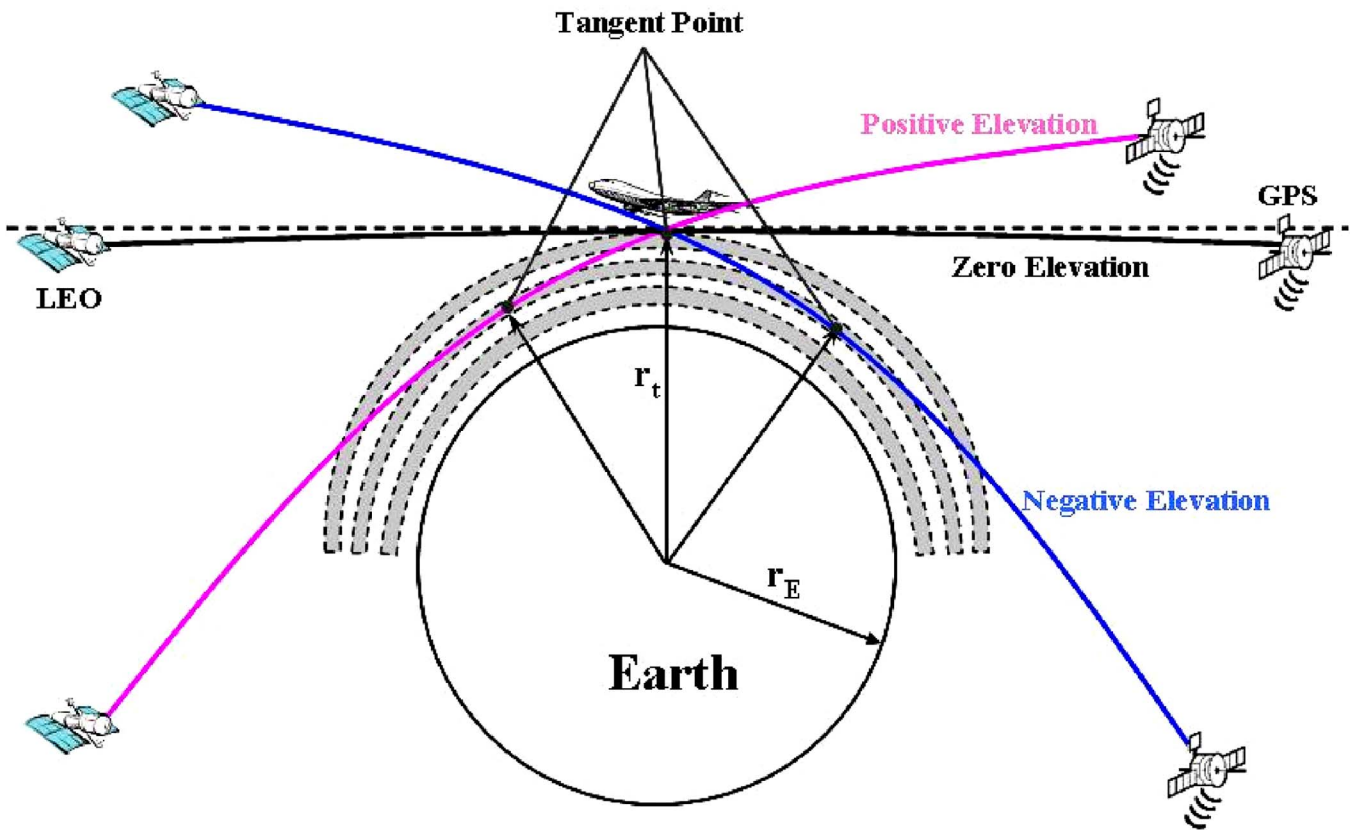

Schematic diagram of the GPS radio occultation geometry with GPS receivers on an aircraft within the atmosphere, an extension of the highly successful atmospheric profiling technique developed for low Earth orbiting satellites.

Profiling the Atmosphere Using the Airborne GPS Radio Occultation Technique: A Sensitivity Study

Feiqin Xie, Jennifer S. Haase, and Stig Syndergaard

***Abstract*—Global Positioning System (GPS) radio occultation (RO) sounding, with its high vertical resolution temperature and humidity profiling capability, is revolutionizing atmospheric science, particularly through assimilation in numerical weather prediction (NWP) models. Currently, the observations are derived from GPS receivers onboard low Earth orbiting satellites. However, with the current number of satellites, it is difficult to provide dense sounding measurements in a specific region within a limited time period. With a GPS receiver onboard an airplane, the GPS RO technique offers such an opportunity while retaining the high vertical resolution sounding capability. The GNSS Instrument System for Multistatic and Occultation Sensing is currently under development for the National Science Foundation's High-performance Instrumented Airborne Platform for Environmental Research (HIAPER) aircraft. This paper presents a sensitivity analysis of the airborne occultation technique that will be used for the HIAPER system. The results demonstrate an anticipated overall accuracy of better than 0.5% for the retrieved refractivity from the surface to about 1 km below the airplane, where the expected airplane velocity errors of up to 5 mm/s limit the accuracy. The effects on the retrievals due to horizontal variations in atmospheric refractivity are significant, and retrieval errors may reach several percent inside frontal systems when the front is perpendicular to the ray paths and within 200 km of the tangent point. In general, the airborne GPS RO system provides a promising new data source for NWP and targeted observational studies.**

***Index Terms*—Airborne, aircraft, atmospheric measurements, Global Positioning System (GPS), microwave radio propagation, radio occultation (RO).**

I. Introduction

THE RADIO occultation (RO) technique is a powerful approach that was developed in the 1960s for investigating planetary atmospheres [1]. In 1995, the first RO measurement of the temperature and humidity in the Earth's atmosphere was successfully acquired using the Global Positioning System (GPS) signals during the GPS/MET mission [2], [3]. A mean accuracy of less than 1 K between 1- and 40-km altitudes and a standard deviation of 2–3 K were achieved with GPS/MET [3]. Since then, many follow-up GPS RO missions have been successfully launched, such as the Challenging Minisatellite Payload (CHAMP) [4], SAC-C [5], and the six-satellite Constellation Observing System for Meteorology Ionosphere and Climate (COSMIC) [6]–[8]. Together, these satellites now provide up to 3000 profiles globally every day. Several features of the GPS RO technique, such as global coverage, high vertical resolution, high precision and accuracy, and the ability of GPS signals to penetrate clouds, have made the RO measurements an extremely valuable asset for global weather forecasting and climate modeling studies [9]–[11]. However, due to the relatively limited number of available low Earth orbit (LEO) satellites, the sampling in a region of specific interest is still rather sparse (only about 1 daily occultation per 167 000 km^2 at midlatitudes and even fewer in the tropics), and it is difficult to acquire a series of profiles that is sequential in time for a desired period. RO measurements with a GPS receiver onboard an airplane offer the opportunity of rather dense sampling contiguous in space and time while retaining a high vertical resolution sounding capability which could greatly facilitate studies of regional weather and climate.

An early work developed a retrieval technique for a receiver on a mountaintop [12] which has a similar geometry to that of an airborne receiver. The retrieval technique has been adapted to airborne measurements, and simulation studies have been carried out by several authors [13]–[15]. A number of field campaigns have also been conducted, and preliminary comparisons of measurements with radiosonde observations and numerical weather prediction (NWP) model analyses have been reported [16]–[18]. Although these preliminary measurements were roughly in agreement with the reference profiles, many different factors could contribute to the errors seen in airborne GPS RO measurements, such as the complicated aircraft motions, the tangent point drifting over a wide range, and horizontally inhomogeneous atmospheric structures. A comprehensive study of the RO retrieval errors due to various sources of observation system error has not been fully described.

In this paper, we apply an end-to-end simulation system to investigate and isolate different error sources and their contributions to the refractivity retrieval errors. This is a preliminary step in assessing the expected error for the development of an operational airborne measurement system. Such a system is under development for the National Science Foundation's High-performance Instrumented Airborne Platform for Environmental Research (HIAPER) with improved capabilities

Manuscript received September 2, 2007; revised February 27, 2008 and June 23, 2008. Current version published October 30, 2008. This work was supported in part by the National Science Foundation under UCAR Contract S05-39696 and in part by the National Aeronautics and Space Administration under Grant 521 13970250 NRA 03-OES-02.

F. Xie was with the Department of Earth and Atmospheric Sciences, Purdue University, West Lafayette, IN 47907-2051 USA. He is now with the Jet Propulsion Laboratory, California Institute of Technology, Pasadena, CA 91109 USA (e-mail: Feiqin.Xie@jpl.nasa.gov).

J. S. Haase is with the Department of Earth and Atmospheric Sciences, Purdue University, West Lafayette, IN 47907-2051 USA (e-mail: jhaase@purdue.edu).

S. Syndergaard was with the COSMIC Project Office, University Corporation for Atmospheric Research, Boulder, CO 80307 USA. He is now with the Danish Meteorological Institute, 2100 Copenhagen, Denmark (e-mail: ssy@ucar.edu).

Color versions of one or more of the figures in this paper are available online at http://ieeexplore.ieee.org.

Digital Object Identifier 10.1109/TGRS.2008.2004713

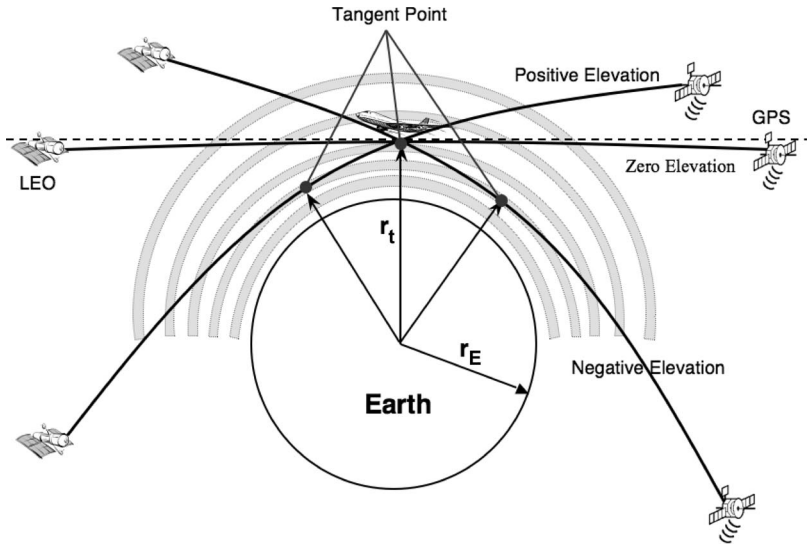

Fig. 1. Schematic diagram of RO geometry with a receiver inside (aircraft) and outside (LEO) the spherically symmetrical atmosphere (shaded). The solid lines connecting the GPS with the airplane represent three ray paths going through the atmosphere with different elevation relative to the local horizon (dashed), where $r_{\rm E}$ and $r_{\rm t}$ are the radius of the Earth and the radius at the tangent point, respectively. The bending of the ray paths and the relative scales of the plot are exaggerated for illustration purposes.

compared to previous airborne GPS RO tests [19]. The GNSS Instrument System for Multistatic and Occultation Sensing (GISMOS) contains two side-looking high-gain antennas with dual-frequency Trimble NetRS GPS receivers, an Applanix POS-AV inertial navigation system with a dual-frequency Trimble BD950 receiver card and an inertial measurement unit, and a GNSS signal recording system capable of continuous sampling of both L1 (1575.42 MHz) and L2 (1227.60 MHz) frequencies at 10 MHz [20] and a Symmetricom 6000 quartz reference oscillator to synchronize the Trimble receivers and the 10-MHz recorder. The retrieval errors of this airborne system, in particular, will be assessed. Section II describes the theoretical basis for the airborne GPS RO measurements, and Section III introduces an end-to-end simulation system based on geometrical optics and describes the accuracy of the airborne RO refractivity retrieval. Some conclusions on the estimated accuracy of the system and a discussion of its limitations are presented in Section IV.

II. Theoretical Basis for the Airborne GPS RO Measurements

GPS RO senses the atmosphere using GPS radio signals that traverse the atmosphere as a moving receiver sets behind the horizon relative to the transmitting satellite. The radio wave is refracted, and its travel time is delayed due to variations of refractivity. A schematic plot of the GPS RO geometry for a LEO and airborne receiver is shown in Fig. 1. The theory for spaceborne GPS RO has been described by several authors [21]–[24]. Here, we summarize the main points of the theory.

The basic measurement is the GPS carrier phase recorded at the receiver, or equivalent distance, subject to a constant offset. Given precise orbits of the GPS transmitters and the location of the receiver, the so-called excess phase is calculated as the difference between the measured phase and that predicted for a vacuum. The excess phase must be corrected for GPS and receiver clock errors. The excess phase is differentiated with respect to time to give the excess Doppler shift, which, in turn, is used to derive the bending angle as a function of tangent altitude [23]. The tangent altitude is at the point of the ray's closest approach to the surface.

Under the assumption of a spherically symmetric atmosphere, Bouguers law [25] states that for a ray passing through the atmosphere, $a = nr\sin\phi =$ constant for any point on that ray at distance r from the center of the earth. Here, n is the refractive index at r and ϕ is the angle between the ray vector and the radial direction at that point. For the LEO case with the receiver outside the atmosphere, the refractive bending angle α as a function of $a = n_{\rm t} r_{\rm t}$, where $r_{\rm t}$ is the curvature radius of the atmosphere at the tangent point, is given as [1]

$$\alpha(a) = -2a \cdot \int_{r_{\rm t}}^{\infty} \frac{1}{n}\frac{dn}{dr}\frac{dr}{\sqrt{(nr)^2 - a^2}}. \tag{1}$$

The refractive index profile $n(a)$ can be derived from (1) via the Abel transform [1]

$$n(a) = \exp\left[\frac{1}{\pi}\int_{x=a}^{\infty}\frac{\alpha(x)dx}{\sqrt{x^2 - a^2}}\right]. \tag{2}$$

Unlike the spaceborne GPS RO case, the airborne GPS RO measurements must be corrected for the asymmetric sampling geometry because the GPS receiver is located inside the Earth's atmosphere. Rays that reach the receiver from above (positive elevation angle) and below (negative elevation angle) the local horizon are all affected by the atmospheric refractivity, but it is not possible to retrieve information unambiguously from the positive elevation angle rays.

For an occultation ray with elevation angle below the local horizon, the bending angle measured at the receiver is

theoretically given by [13]

$$\alpha_{\mathrm{N}}(a) = -2a \cdot \int_{r_{\mathrm{t}}}^{r_{\mathrm{R}}} \frac{1}{n}\frac{dn}{dr}\frac{dr}{\sqrt{(nr)^2 - a^2}} - a \cdot \int_{r_{\mathrm{R}}}^{r_{\mathrm{T}}} \frac{1}{n}\frac{dn}{dr}\frac{dr}{\sqrt{(nr)^2 - a^2}}. \tag{3}$$

This is an integral along the ray path from the receiver to the tangent point altitude, continuing backup to the altitude of the receiver, and then continuing from the altitude of the receiver to the GPS satellite. In (3), r_{T} and r_{R} refer to the radii of the transmitter and receiver altitudes, respectively, and r_{t} is the radius at the tangent altitude. The constant a, for a given ray, is known as the impact parameter. Assuming a spherically symmetric atmosphere, for every negative elevation angle ray, with bending angle α_{N}, there is a corresponding positive elevation angle ray, with bending angle α_{P} with the same impact parameter, which is, in fact, equal to the second term in (3). These two bending angles can be subtracted to retrieve the so-called "partial bending angle." The partial bending angle corresponds to the accumulated bending from a segment of the ray path below the altitude of the receiver

$$\alpha'(a) = \alpha_{\mathrm{N}}(a) - \alpha_{\mathrm{P}}(a) = -2a \cdot \int_{r_{\mathrm{t}}}^{r_{\mathrm{R}}} \frac{1}{n}\frac{dn}{dr}\frac{dr}{\sqrt{(nr)^2 - a^2}}. \tag{4}$$

The refractive index below the receiver can then be retrieved through the slightly modified Abel transform [13] which is similar to the spaceborne GPS occultation case, but the refractive index at the receiver n_{R} can no longer be neglected

$$n(a) = n_{\mathrm{R}} \exp\left[\frac{1}{\pi}\int_{x=a}^{n_{\mathrm{R}} r_{\mathrm{R}}} \frac{\alpha'(x)dx}{\sqrt{x^2 - a^2}}\right]. \tag{5}$$

The refractive index profile is transformed to a function of altitude rather than impact parameter using the relation $a = nr$ at the tangent point where $\phi = 90^\circ$. In practice, α_{N} and α_{P}, as functions of a, are derived from the measured excess Doppler shifts in a similar way to that used for the spaceborne case.

The refractivity at GPS frequencies, defined as $N = (n-1) \times 10^6$, depends on atmospheric pressure (P in hectopascals), temperature (T in kelvins), and water vapor partial pressure (P_{w} in hectopascals) through the following relation [26]:

$$N = 77.6\frac{P}{T} + 3.73 \times 10^5 \frac{P_{\mathrm{w}}}{T^2}. \tag{6}$$

Consequently, the atmospheric thermodynamic parameters, such as density, temperature, pressure, and humidity, can be inferred based on the GPS RO refractivity retrievals. In the upper atmosphere or near the poles, the effect of moisture may often be neglected to solve for temperature directly. Otherwise, a first guess temperature profile may be used to solve for humidity, or the humidity and temperature can be solved for simultaneously using 1-D variational analysis [21], [27], [28].

III. Sensitivity Analysis of the Retrieval System

A. Simulation System

In order to investigate the performance of the airborne GPS RO measurements, a simulation system based on geometrical optics was developed, as shown in Fig. 2. The simulation system includes four main components: 1) a geometrical optics ray tracer, which simulates the GPS signal as it travels through a given atmospheric refractivity model; 2) a module that derives the bending angle from the excess Doppler measurements; 3) a forward integrator that generates the bending angle profile through the forward integration [see (3) and (4)] of an input 1-D refractivity profile; and 4) an inverse integrator that retrieves a refractivity profile via Abel inversion using (5). There is an option to add errors at any step in the forward simulation system. By comparing the retrieved refractivity profiles with the input profile, we quantitatively evaluate the refractivity errors due to various factors such as the measurement errors in the excess Doppler and error in the *in situ* observation of refractivity at the receiver. We also assess errors due to the assumption of spherical symmetry, which is violated in cases of strong horizontal refractivity gradients.

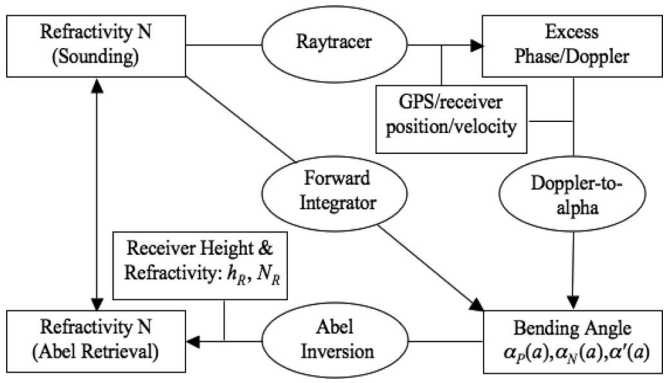

Fig. 2. Geometrical optics simulation system.

For illustration of the simulation system, we input a 1-D exponential model [Fig. 3(a)] of atmospheric refractivity with a fixed scale height ($H = 7$ km), such that $N(h) = N_0 \cdot e^{-h/H}$, where h is the altitude and $N_0 = 385.84$ (N-unit) is the refractivity close to the surface. We also specify a simple occultation geometry (similar to Fig. 1) with a GPS satellite setting behind the horizon in a circular orbit at 20 000 km above the surface, while the airplane is flying at a fixed 10-km altitude above the surface of a spherical Earth with radius $R_{\mathrm{E}} = 6370$ km in the same plane as the GPS orbit. The GPS satellite and the airplane velocities relative to the stationary Earth are set to $v_{\mathrm{GPS}} = 3.83$ km/s and $v_{\mathrm{AP}} = 0.25$ km/s (or 900 km/h), respectively.

In these simulations, the ionospheric effect is neglected and only the L1 signal is simulated, assuming that the observations can be corrected for ionospheric effects with minimal errors. Note that for a spherically symmetrical ionosphere, the ionospheric refraction cancels when subtracting α_{P} from α_{N} [13]. The excess phase as a function of time as the GPS satellite sets (the aircraft moves relatively little compared to the GPS satellite) is shown in Fig. 3(c). At around 205 s, the GPS is at about 3.2° above the horizon, where it is necessary to begin measuring the positive elevation bending angle to be paired with the negative elevation bending measurements later on. The excess phase at this time is 10.1 m, which is clearly much bigger than the typical relative GPS positioning error. The differentiated excess phase (the excess Doppler) increases rapidly as the ray descends deeper into the atmosphere with time [Fig. 3(d)].The corresponding bending angle profile as

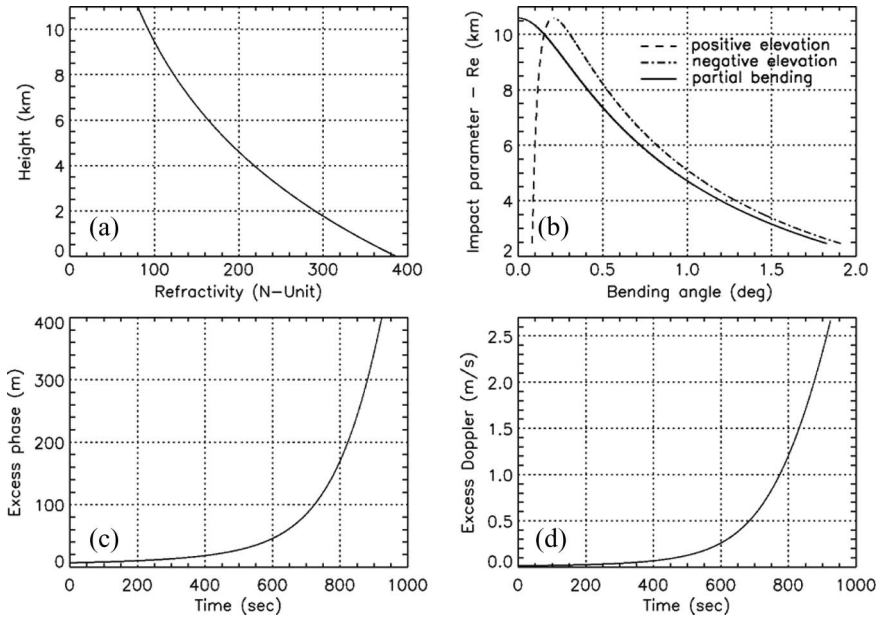

Fig. 3. (a) Exponential refractivity model with fixed 7-km scale height. (b) Bending angle as a function of impact parameter for a receiver located at 10-km altitude (the radius of the Earth $R_{\rm E} = 6370$ km). Solid line shows the partial bending angle, which is the difference between (dashed-dotted) negative elevation bending angle and (dashed) positive elevation bending angle. (c) Excess phase as a function of time. (d) Excess Doppler as a function of time.

a function of impact parameter is shown in Fig. 3(b). The lowest bending angle corresponds to the highest elevation angle ray above the horizontal (starting at about 3.2°). The positive elevation bending angle increases slowly as the ray descends toward the horizontal, roughly as the inverse of the sine of the elevation angle, until it reaches the maximum impact parameter, $a_{\rm R} = n_{\rm R} r_{\rm R}$ at the horizontal. The negative elevation bending angle increases rapidly as the impact parameter decreases. Also shown in Fig. 3(b) is the partial bending angle, which is the difference between the negative and positive elevation bending angles. The partial bending angle can then be inverted to retrieve the refractivity using the Abel transform [see (5)].

B. Retrieval Errors Due to Aircraft Velocity Uncertainty

The largest error we expect from the observing system is the error associated with velocity errors in the navigation system, which map directly into the Doppler data. The Applanix POS-AV on the HIAPER GISMOS system has a specified rms velocity error of 5 mm/s [20]. Preliminary tests were carried out by postprocessing the Applanix GPS data from a test flight using different ground-based GPS reference stations. When the solutions were compared, the differences were consistent with the specified error. In this simulation, randomly generated errors with a standard deviation of 5 mm/s are added to the Doppler time series. The bending angle is then calculated from the noisy Doppler data.

One-hundred realizations of random noise with zero mean and 5-mm/s standard deviation were added to the Doppler profile, sampled at 1 s, to determine the distribution of errors in the derived bending angle and refractivity. The mean and standard deviation in the percent error as a function of impact parameter for the partial bending angle are shown in Fig. 4(b). The fractional errors increase near the altitude of the aircraft because the accumulated refractive bending is small.

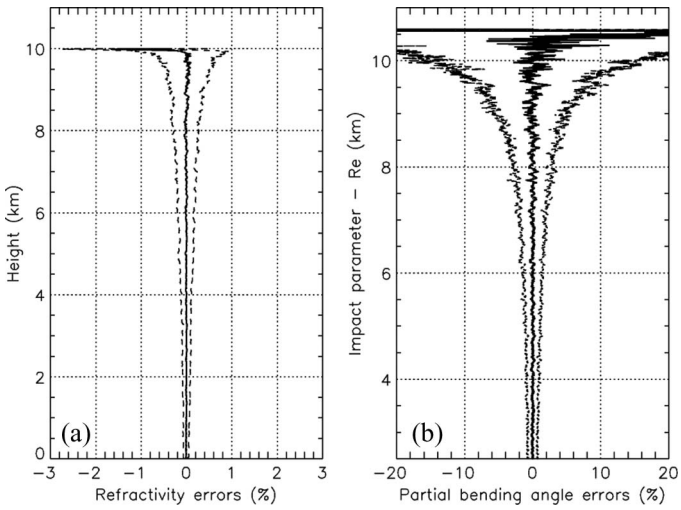

Fig. 4. (a) Fractional refractivity retrieval errors of the airborne GPS RO measurements due to a random excess Doppler error (zero mean and standard deviation of 5 mm/s). (b) Corresponding fractional partial bending angle errors. Note that mean error is in solid line and standard deviation is in dashed lines for both panels.

The distribution of the errors in the retrieved refractivity as a function of altitude is shown in Fig. 4(a). As with the bending angle, errors in refractivity increase with altitude near the aircraft altitude. Above 9 km, the refractivity retrieval errors due to the 5-mm/s velocity error in the Doppler exceed 0.5%, which corresponds to about 1 K at 10 km, but do not become much larger than 1%. This error level is comparable to that of radiosondes, and therefore, the observations are of sufficient quality to provide an attractive supplement to the existing upper air sounding system. The target accuracy of 0.5% or 1 K at 10 km is the requirement for operational sounding by the spaceborne missions [29], [30]. Useful information could still be retrieved above these altitudes, but the Doppler data would have to

be averaged over a longer time period, producing reduced height resolution in the profile. Any reduction in Doppler error effectively increases the height range over which observations can be reliably retrieved. The altitude at which the errors exceed 0.5% also depends on the flight altitude of the aircraft. These tests were carried out at 10 km because that is the typical flight level of commercial aircraft. The HIAPER aircraft can fly up to 15 km and will have more accurate observations at 10 km than the examples reported here.

Based on preliminary flight test data with the Applanix system, there are occasionally periods where there is a trend in the velocity error that could be as much as 3 mm/s over a period of 2000 s. This correlated error will introduce a much larger error in the retrieved refractivity compared with the random errors. After adding such an error distribution to simulated observations, the resulting retrievals from the Abel transform have a positive bias (0.2∼1%) (figure not shown). This is an unacceptably large bias. However, performing the multiple velocity solutions appears to be a useful method of quality control, in order to detect times when this would be a problem. In these test flights, these periods did not occur often but were associated with rapid and large changes in flight altitude. During operational measurements, variations in altitude will be limited, so these periods are anticipated to be rare. Outside these periods, the velocity error appeared to be random.

C. Retrieval Errors Due to Aircraft In Situ Refractivity Uncertainty

The Abel inversion [see (5)] requires measurement of the refractive index at the aircraft n_{R}. The HIAPER aircraft is equipped with several instruments to sample the *in situ* temperature and relative humidity [19]. Due to the very limited contribution of the humidity to the refractivity at 10 km, the error in the *in situ* refractivity depends primarily on errors in the *in situ* temperature measurement. A typical value of 1-K *in situ* temperature measurement error results in less than 0.5% refractivity error. The effect of *in situ* temperature measurement errors was simulated by superimposing 0.5% random refractivity errors on the assumed refractivity at the aircraft altitude in the Abel inversion. Because the refractivity at the top of the profile affects all the rays with tangent points at all altitudes, there is an altitude-dependent effect in the resulting refractivity profile. From 100 realizations of this error, the retrieval error profile was created (Fig. 5). The resulting errors reach up to 0.2% at the heights nearest the aircraft and decrease to 0.05% at 9.9 km and become even smaller below, which is much smaller than the retrieval errors due to the velocity uncertainties. Note that there is a small negative bias below 5 km with a maximum (0.02%) at the surface and that there is also a very small positive bias near the aircraft altitude. We believe that these biases are caused by the algorithm to compute the bending angle from the Doppler measurements. However, the biases are almost an order of magnitude less than the retrieval errors due to the velocity uncertainties. Thus, it will not have a noticeable effect on the simulation results presented in this paper.

An accuracy of about 0.3 hPa for the *in situ* pressure measurement can be achieved onboard of the airplane, which corresponds to about 0.1% refractivity error at 10-km altitude according to (6). It is less significant compared with the *in situ* temperature measurement error. At higher altitudes (e.g., 15 km), 0.3 hPa will result in about 0.3% refractivity error and is comparable to the temperature error and would have the same behavior as that shown for temperature in Fig. 5.

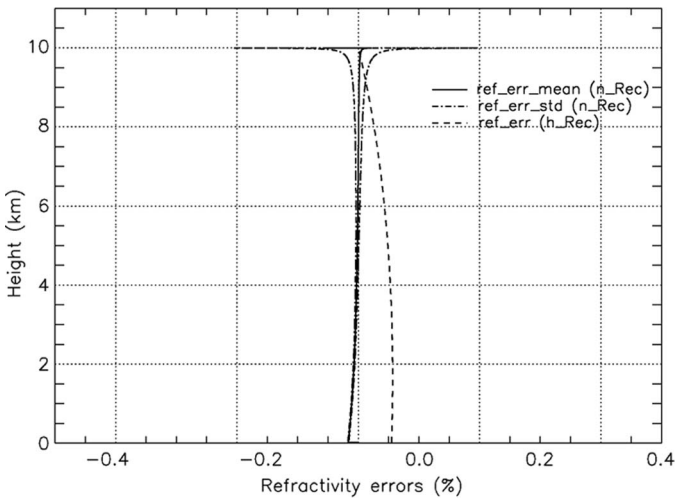

Fig. 5. Fractional refractivity retrieval errors due to a random refractivity error (0.5%) at the receiver (mean error in solid and standard deviation in dash-dotted lines). The dashed curve shows the fractional refractivity error due to a change in receiver altitude (ascending) during a setting occultation measurement.

There is some evidence that aircraft observations of *in situ* temperature, in particular for operational reporting from commercial aircraft, are biased by up to 0.7 K [31]. This result was obtained with assimilation tests using LEO satellite GPS occultation data. The biased *in situ* measurement will introduce bias into the occultation refractivity retrieval based on the Abel inversion in (5). However, as shown in Fig. 5, the impact of the *in situ* measurement error is very much restricted to the altitudes close to the receiver and decreases sharply at lower altitude. We should therefore still expect to get unbiased retrievals from the surface and up to one kilometer below the receiver.

During the occultation, if there is a change in aircraft altitude, then there is a difference in the *in situ* refractivity measured at the time the positive and negative elevation angles are observed. More importantly, in this situation, the aircraft is no longer at a constant height above the Earth's surface, which is assumed in the derivations of (4) and (5). To assess the error due to variation in flight altitude, a simulation was run with the aircraft starting below 10 km and increasing slowly in altitude at a rate of 1 m/s so that over the course of a 12-min setting occultation, the altitude varied by approximately 720 m. The simulation was planned so that at the time of the zero elevation angle measurement, the aircraft is exactly at 10-km altitude. In this case, both the positive and negative elevation angle rays will have additional accumulated bending (or positive bending bias accumulated between the receiver altitude and the reference level, i.e., 10 km) compared to the corresponding bending measurements with a receiver at the fixed reference level. According to (4), the partial bending angle is the difference between a pair of negative and positive elevation bending angles at the same impact parameter. Note that it takes less occultation time to cover the positive elevation angle range compared to

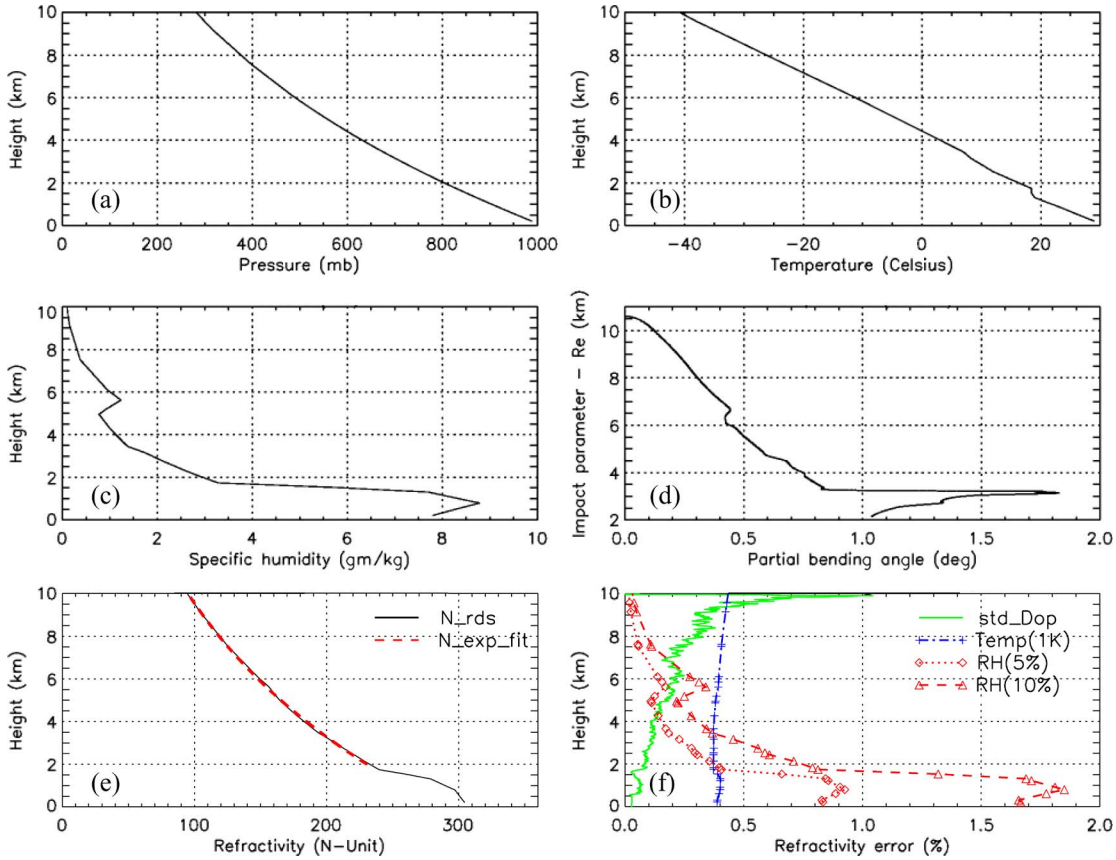

Fig. 6. Radiosonde profile from Green Bay, Wisconsin, at 2007080300Z. (a) Pressure. (b) Temperature. (c) Specific humidity. (d) Partial bending angle. (e) Refractivity profile (solid) and a best fitting exponential profile (between 2 and 10 km, bold-dashed). (f) Standard deviation (solid) refractivity errors due to 5-mm/s Doppler error. Also shown in (f) is the equivalent refractivity error to current observational accuracy of 1-K temperature error (dash-dotted and plus), 5% humidity error (dotted and diamond), and 10% humidity error (dashed and triangle).

the negative elevation angle range. Therefore, with a constant ascent rate, the receiver is further away from the reference level in the negative elevation bending compared with that of the positive elevation measurement at the same impact parameter. For smooth refractivity profiles, the positive bias in the negative elevation bending is thus systematically larger than that in the corresponding positive elevation bending, which will lead to a positive bias in the partial bending and, thus, a positive bias in the Abel-retrieved refractivity. Similarly, if the aircraft is descending, the partial bending angle bias will be negative, resulting in a negative refractivity bias.

In the simulation, the bending angles were inverted using an Abel inversion, assuming that the receiver altitude was constant at 10 km and using the value of n_{R} at this altitude. The resulting error in retrieved refractivity is shown in Fig. 5 (dashed). The error is positive in this case, as expected, because the aircraft altitude is increasing. The error is quite small (less than 0.06%) compared with other sources of error shown in Fig. 4. The requirement that the aircraft altitude does not vary by more than 720 m is easily assured in practice, so this error is not expected to be significant.

D. Retrieval Errors in a Moist Atmosphere

A retrieval error simulation using a radiosonde profile with a more complicated vertical structure illustrates several other important points. Radiosonde measurements of humidity are subject to biases when rising through layers with a sharp drop in humidity, because of the delayed response of the sensor, or when exiting a cloud layer where the air is saturated [32]. The radiosonde profile chosen from Green Bay, Wisconsin, on 00:00(UTC) August 3, 2007 is used to demonstrate whether the same level of accuracy is achievable for a typical profile with a large range of moisture variation. Pressure, temperature, specific humidity, and the derived refractivity from the profile are shown in Fig. 6. There is a sharp temperature and humidity change at the top of the boundary layer at 1.8 km and a sharp increase in moisture at about 5 km. These features are clear even in the refractivity profile in Fig. 6(e). Forward modeling with a geometrical optics ray tracer is problematic for the sharp boundary layer gradient, because atmospheric multipath and diffraction cause the phase to vary wildly [33], [34]. Therefore, in this case, the forward Abel integrator [see (5)] is used to simulate the bending angle profile. For real data, several techniques are available to mitigate the effects of the multipath and will be discussed further in Section IV. The partial bending angle is also shown in Fig. 6(d). The extreme increase in bending angle indicates the existence of a sharp boundary layer, where a small change in impact parameter generates a large variation in bending.

To simulate the effects of velocity noise, we superimpose random fluctuations in the partial bending angle from Fig. 4(b) (equivalent to 5-mm/s Doppler errors) onto the partial bending angle derived from the radiosonde [Fig. 6(d)]. One hundred

profiles were simulated, and the retrieval statistics are shown in Fig. 6(f) (solid). The relative differences between the radiosonde profile and the best fit exponential profile (from 2 to 10 km) vary by over 1% (not shown), which is much larger than the Doppler-introduced refractivity retrieval errors, particularly below 7 km. This illustrates the relative importance of the errors related to the variations in the profile that are of most interest. The upper level drying and sharp moisture increase at 5–6 km, which are rather subtle features (1.3% variation) in the refractivity profile, are still much larger than the refractivity retrieval error of about 0.2%. This indicates that such features can still be retrieved even when the data are affected by Doppler noise.

An intercomparison of high-quality radiosonde systems shows a typical 4%–6% humidity measurement error compared to reference radiosondes [35] with the error in some situations as high as 10%. Therefore, we used 5% humidity error to represent the current state-of-the-art *in situ* humidity measurement error from radiosondes with a 10% upper bound. NWP model analyses can have typical temperature errors of 1 K from surface to the lower stratosphere and have background errors in relative humidity in the upper troposphere as large as 20%–50% (Loïk Berre at Météo France, personal communication) and at best 10% at the surface (Sean Healy at ECMWF, personal communication). Therefore, we use 10% humidity and 1-K temperature errors to represent the lower bound model analysis errors. These limits are shown in Fig. 6(f), with lines that indicate the refractivity error corresponding to a 5% error in humidity, a 10% error in humidity, and a 1-K error in temperature calculated from (6). Comparing these with the altitude-dependent error in the refractivity retrieval gives an indication of when the RO observations are accurate enough to provide an improvement in observation accuracy over currently available observations and analysis quality. Therefore, the retrieved profiles will be most useful in providing temperature information (better than 1 K) up to an altitude of about 9 km (or 1 km below the airplane) and relative humidity information up to about 5 km (better than 5%) or up to about 7 km (better than 10%).

E. Vertical Resolution

One of the advantages of the RO technique is the high vertical resolution of the profiles. The vertical resolution is defined by the diameter of the first Fresnel zone Z_{F} at the ray tangent level [21]. In the absence of significant atmospheric bending, this limit for the airborne case can be calculated as follows [14]:

$$Z_{\mathrm{F}} = \sqrt{2\lambda\left(\frac{L_{\mathrm{T}}L_{\mathrm{R}}}{L_{\mathrm{T}}+L_{\mathrm{R}}}\right)} \approx \sqrt{2\lambda L_{\mathrm{R}}} \qquad \text{if } L_{\mathrm{T}} \gg L_{\mathrm{R}} \quad (7)$$

where λ is the GPS signal wavelength, L_{T} is the distance from the transmitter to the limb, and L_{R} is the distance from the limb to the receiver. The GPS L1 wavelength is about 19 cm, L_{T} is approximately 25 800 km, and L_{R} may be on the order of 360 km for the lowest point of the profile; therefore, (7) gives a value for the maximum vertical resolution of 0.37 km for Z_{F}. For a spaceborne occultation, the vertical resolution is 1.4 km in the absence of significant atmospheric bending [21]. If we take into account the vertical refractivity gradient, (7) is multiplied by a defocusing factor, and the first Fresnel zone is defined by the expression

$$Z_{\mathrm{F}} = \sqrt{\frac{2\lambda L_{\mathrm{R}}}{1+L_{\mathrm{R}}\frac{\partial\alpha}{\partial a}}}. \quad (8)$$

When the vertical gradient increases, the diameter of the first Fresnel zone decreases, and the vertical resolution improves. For a spaceborne occultation, the vertical resolution in the lower troposphere is generally better than 500 m, taking into account the defocusing factor. In a region with large vertical refractivity gradients such as the top of the boundary layer, the vertical resolution improves over the case with no bending. In Figs. 3 and 6, $\partial\alpha/\partial a$ is approximately 0.1–$0.2^{\circ}/\mathrm{km}$. This leads to a first Fresnel zone equal to 200–240 m. A vertical sampling interval of 240 m corresponds to approximately a 10-s interval below 8 km; therefore, the required sampling rate for the receivers is then for half that interval, 5 s, or 0.2 Hz. However, in a region where there is atmospheric multipath, the sampling rate would need to be higher than 0.2 Hz. Observations in the presence of atmospheric multipath would require an open-loop tracking receiver, which would be capable of much higher sampling rates. The system developed for HIAPER has a receiver that samples at 5 Hz, which is expected to perform well at least under conditions when atmospheric multipath is absent.

F. Effects of Horizontal Structure

The horizontal drift of the airplane tangent point is somewhat larger for an airborne case than for a space-based receiver because the receiver is moving at a much slower speed than the transmitter. The errors due to the spherical symmetry assumption in the presence of significant horizontal gradients are compounded by the horizontal drift of the tangent point. To quantify these errors, we carried out simulations using refractivity fields that approximate the horizontal and vertical temperature and humidity gradients found in a typical frontal system. Rays were traced through a 2-D structure from the aircraft altitude to the altitude of the GPS satellite. The bending angles were calculated, the positive elevation angle bending was subtracted from the negative elevation angle bending, and the bending angle was inverted to obtain the refractivity. We note that these simulations include the lateral variations above the aircraft height, i.e., the positive elevation angle bending was taken from a ray sampling a different type of structure than the negative elevation angle ray.

The frontal disturbance is approximated with an idealized model using analytic formulas for a sloping change in the refractivity of the atmosphere, where the meridional and zonal gradients of the front are also variables [36], [37]. In these cases, both the meridional and zonal gradients are varied and the front slope is set to 2%. A typical value of the frontal slope in the real atmosphere is 1% but becomes larger and may reach 5% close to the surface. Cross sections of pressure, temperature, specific humidity, and refractivity are shown in Fig. 7.

The horizontal variations will affect the bending angle profile differently depending on the position and orientation of the weather front relative to the tangent point drifting path. Fig. 8 shows the geometry of different test cases that were carried out.

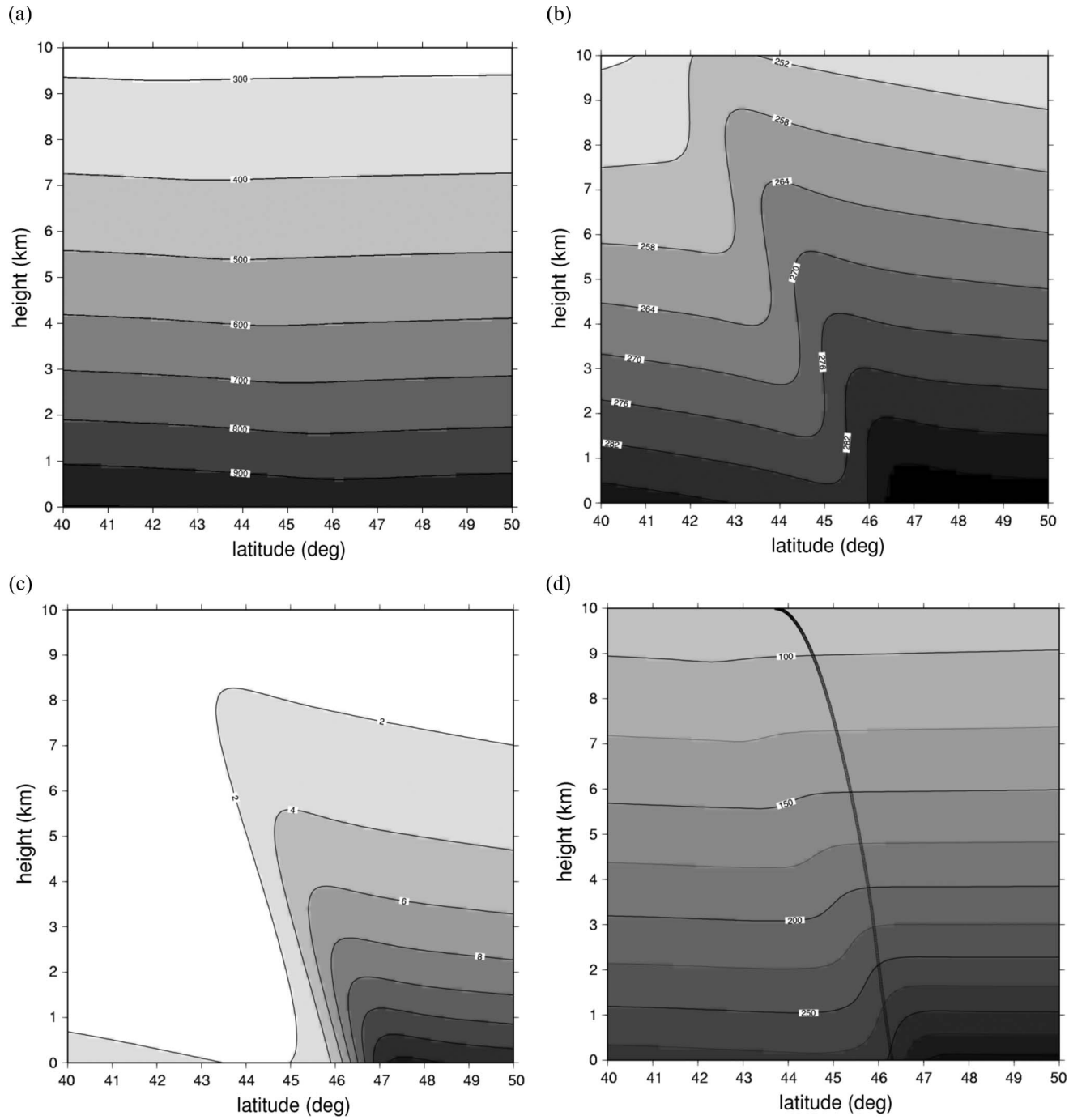

Fig. 7. Cross sections of the model weather front. The surface position of the front is located at 45° N, and the orientation of the front is perpendicular to the ray paths (corresponding to the middle position of the front in Fig. 8). The four contour plots are (a) pressure (in hectopascals), (b) temperature (in kelvins), (c) specific humidity (in grams per kilogram), and (d) refractivity (N-units) with the tangent point locations of the ray paths superimposed.

The ray paths from the GPS satellite to the aircraft receiver are in a single plane along the 90° W line. A total of ten cases were simulated. Four cases with fronts oriented north, east, south, and west relative to the center of the tangent points are indicated by the open triangles. Another six cases with the front oriented north (i.e., front is perpendicular to the ray path with cold air in the south and warm air in the north) were added. All the six fronts were centered at 90° W with different latitudes. For clarity, only the front located at 45° N, 90° W was shown in the black solid triangles in Fig. 8. Note that in all the simulations, the occultation geometry is fixed, with the airplane flying from north to south, and the tangent point is drifting from south to north along 90° W longitude.

For the first case, the front indicated by black solid triangles is perpendicular to the ray path. The circles in Fig. 8 show the tangent point locations of negative elevation ray paths during the occultation event. The tangent point drifts from 43.7° N (at the receiver altitude) to 46.3° N when the tangent point touches the surface.

The bending angle is most sensitive to the refractivity at the tangent point. However, with these lateral variations, the refractivity assigned to the estimated tangent points will be

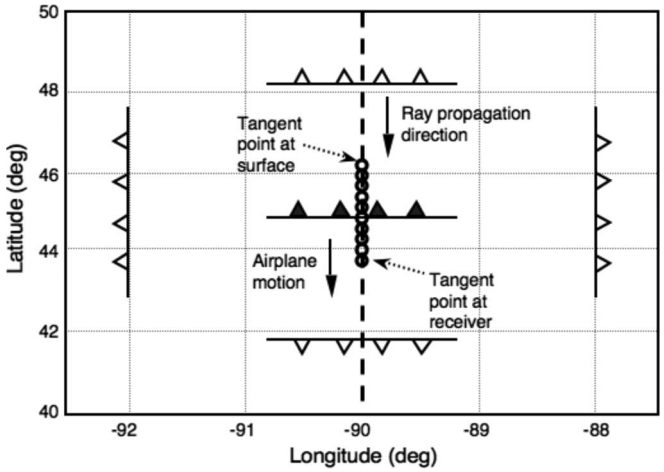

Fig. 8. Ray paths (north to south) and front locations in latitude–longitude coordinates. The south-end ray tangent point corresponds to a ray tangent altitude at 10 km, and the north-end ray has its tangent point close to the surface. The lines with triangles indicate the surface positions and orientations of the front for five separate occultation simulations. The front with the black solid triangles corresponds to the case shown in Fig. 7, whereas the fronts with open triangles represent the four other cases. The circles indicate the tangent points for the case shown in Fig. 7.

some weighted average of the values around this point [37]. For comparison, we selected the refractivity from the input front model at each of the tangent point locations and call this the model tangent point refractivity profile. The relative refractivity differences between the retrieved profiles and the model tangent point refractivity profiles are shown in Fig. 9. For the simulation with the front located at 45° N perpendicular to the ray paths, the relative refractivity differences are very large at the altitude of 2 km, more than 4.5% (diamond symbols). This is the largest effect, which occurs near the surface very near the front. Above 5 km, the profile errors are less than 0.5%.

The location of the front perpendicular to the ray paths was varied north and south of 45° N. The retrieved refractivity is shown by the six other curves in Fig. 9(a). With the front at 44° N (solid line) and 46.35° N (triangles), the retrieved refractivity has large errors at the most sensitive altitudes. For fronts perpendicular to the ray paths but at further distance, the effect is small (41.7° N, plus; 43° N, stars) on the south side where the slope is dipping toward the tangent point profile. On the north side (48.35° N, squares; 50.35° N, cross) where the slope is dipping away from the tangent point profile, the retrieved refractivity approaches the accuracy of 1%, but with a positive bias.

We also simulated the fronts at four different orientations relative to the ray paths: 1) an E–W front to the north of the tangent point profile, which has been shown in Fig. 9(a) (squares); 2) an N–S front to the east (diamonds); 3) an E–W front to the south (triangles); and 4) an N–S front to the west (plus). The refractivity errors are shown in Fig. 9(b). For fronts oriented parallel to the profile on the moist and dry side of the front at 2° longitude distance from the ray paths (diamonds and plus), the effect is very small, less than 0.02%. Once again, a positive bias (less than 1%) is found in the retrieval when the front is perpendicular to the ray paths with the slope dipping away from the tangent point (triangles).

In the aforementioned simulations, we know the refractivity at the tangent point for comparison. However, in the actual comparison, for example, with a radiosonde observation near the front which is closer to vertical, the differences would appear even greater because of the drift of the tangent point across the front and the integrated effect of the refractivity gradients along the ray path. The retrieved profile is essentially a weighted average of the refractivity field along the ray paths. Thus, direct assimilation of such refractivity measurement into a numerical weather model by interpreting it as a vertical profile or as individual refractivity values at the tangent points at different latitude, longitude, and altitude would misrepresent some of the information in the data. Possible ways of assimilating the occultation data while taking into account the horizontal gradients in the spaceborne case have been developed [11], [38]. These methods can be adapted to the airborne case.

Note that there may be a contribution to the retrieval error due to horizontal variations in refractivity at the aircraft height over the course of the occultation. The refractivity observed at the aircraft location is used in the bending angle calculation for an individual observation. However, only the refractivity observed at the time that the zero elevation angle measurement is made is used as the top refractivity in the Abel inversion integral. This assures that the retrieval error is zero for the refractivity at the top of the profile (10 km). The typical horizontal variation in refractivity over 150 km (10-min occultation with airplane flying at 900 km/h) at 10-km altitude at midlatitudes is about 0.5% and may be systematic along the flight path. Such refractivity variation is about an order of magnitude less compared with the refractivity variation along the fly path in the changing aircraft altitude simulation (Section III-C). Thus, we would expect that the resulting retrieval refractivity error due to the horizontal variation along the fly path is smaller than 0.06% (cf. Fig. 5), which is much smaller than the retrieval error due to velocity uncertainties.

Frontal structures can cause a large difference in two profiles that sample different areas of the structure. It is possible that a set of retrievals from a flight, for example, from a flight plan with a 90° turn that would have occultation ray path sampling in different orientations, could indicate the location or strength of a front just through the differences in structure retrieved in the profiles.

IV. Discussion

Atmospheric attenuation and problems due to atmospheric multipath limit the ability of an RO receiver to acquire and track the signal in the lower troposphere, particularly at the top of the boundary layer where steep vertical refractivity gradients exist. The current simulations are limited by the use of the geometrical optics algorithms. In particular, the ray-tracing algorithm used for calculating the excess phase and Doppler cannot be used below the part of the profile where several ray paths with different impact parameters arrive at the same receiver location. The ray-tracing algorithm would have failed, for example, for the steep boundary layer in the radiosonde profile in Section III-D. Instead, we were able to estimate the accuracy by using a forward Abel integration to get a reasonable estimate of the accuracy.

Several retrieval methods have been developed for inverting observations affected by atmospheric multipath and diffraction

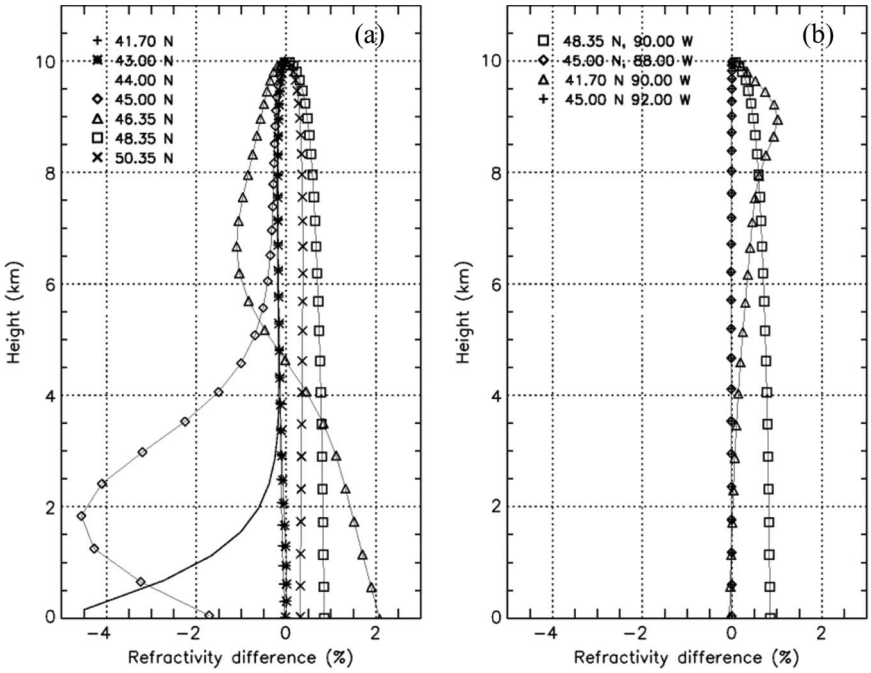

Fig. 9. (a) Fractional refractivity difference of the Abel-retrieved refractivity profile compared with the model tangent point refractivity profile for the front at different latitudes indicated in the legend. The curve with diamond symbols, for example, shows the result for the front located at 45° N, oriented perpendicular to the ray paths. (b) is the same as (a) but for fronts oriented north (square), east (diamond), south (triangle), and west (plus) of the center of the tangent points.

[39]–[41], some of which could be modified for the airborne RO application. In some cases, the amplitude and phase fluctuations are so large that the tracking algorithm of the receiver loses lock, and no data are retrieved beyond this point. This led to a lower limit for retrievals for some of the early satellite missions, such as GPS/MET and CHAMP. However, the SAC-C satellite and the COSMIC satellites are equipped with open-loop tracking receivers, so that some or all of the profile can be recovered even in cases of strong fluctuations. The HIAPER aircraft as well is equipped with a GNSS recording system as part of GISMOS, which records the 10-MHz sampled raw signal. A software receiver can be used to recover the phase and amplitude data using an open-loop tracking algorithm [42]. However, it does not eliminate the problem due to superrefraction, where very sharp vertical refractivity gradients could contribute to the nonuniqueness of the Abel inversion [43]. In this case, additional *a priori* constraint such as the surface refractivity could aid in getting a full retrieval throughout the boundary layer.

Local multipath is a potential error source that is highly dependent on the location of the occultation antenna relative to the airplane wings, as well as the occultation geometry. Past studies on aircraft [44], [45] have shown carrier phase multipath signals on individual satellites that vary slowly on the order of 5–6 cm over time periods of 1000–1800 s, or 0.03–0.05 mm/s. This is much smaller than other noise sources for occultation. These studies were done using GPS data only. When an integrated GPS/INS system is used, the independent IMU data, which are not sensitive to multipath, improve the solution and reduce the impact of the multipath of the GPS environment. Another study of multipath on aircraft [46] based on models of the aircraft structure indicated a high level of multipath contamination with evidence of large SNR variations for a small range from 10° to 30° in elevation and 15° in azimuth. This is a very limited range in which it would be a problem, and is not at very low elevation angles where the occultation measurements are being made. However, any study is very specific to the individual aircraft. It is recommended that the magnitude of the local multipath and its dependence on the orientation between the line of sight and the aircraft orientation should be quantified with test recordings. Such a study would provide a range of orientations for which observations that are likely to be contaminated could be screened.

Clock errors are a potential source of error. The HIAPER system has a Symmetricom 6000 GPS steered oven quartz oscillator as a time reference to provide synchronization between the NetRS GPS receivers and the 10-MHz GPS signal recorder. However, this clock has a stability of 1 part in 10^{11}, so it is not accurate enough to produce uncorrected excess-phase observations. A differencing technique is required to remove these errors. Single differencing the observations with observations to a nonocculting GPS satellite and using clock drift estimates from GPS analysis centers responsible for precise orbit determination will yield excess-phase errors on the order of $\pm$ 2 mm/s [47]. This error is less than the limiting aircraft velocity error.

Ionosphere errors can be corrected using dual-frequency measurements. For the GPS-LEO RO, the ray paths for L1 and L2 signals are separated at the tangent point because of ionospheric dispersion, requiring a correction of bending angles at equal impact parameters [23]. For the airborne case, the L1 and L2 tangent points are very close together because the receiver is much closer to the tangent points. At the same time, ionospheric residual errors are known to be less of a problem at tropospheric altitudes because the angle of incidence between the rays and ionospheric layers is larger than it is at higher altitudes. It is therefore expected that ionospheric residual errors are less of a problem for the airborne occultations, and the more

traditional ionospheric correction of phases should be sufficient and straightforward to apply to the airborne measurements.

V. Conclusion

Through simulations that incorporate realistic measurement system errors, we have estimated the expected accuracy of airborne GPS RO profiles. The primary contribution to the retrieval error is the uncertainty in the aircraft velocity, which, with the current state of the art, is on the order of 5 mm/s. This error maps directly into an error in the Doppler measurement. The retrieved refractivity accuracy is estimated to be better than 0.5% at altitudes less than 1 km below the airplane flying at 10 km, with very little bias. The uncertainty of the *in situ* refractivity needed for the retrieval can lead to an error of less than 0.2% in the retrieved refractivity at the altitudes nearest the aircraft, which is much smaller than the retrieval errors due to the velocity uncertainties. The assumption of spherical symmetry in the bending angle calculation and the Abel inversion is violated when there are strong variations in refractivity due to fronts, for example. Simulations show that the assumption of spherical symmetry can cause errors up to 4.5% in the worst case where the ray paths intersect perpendicular to the front and the tangent point drifts horizontally across the front. However, for cases where the front is more than about 200 km from the tangent point profiles, or parallel to the tangent point profile, the errors are less than the errors due to the velocity error. Several sources of bias in the retrieved refractivity have been identified, and the magnitude of those biases has been estimated. The few biases that exist have been shown to be small enough to be negligible, or large only in the altitude range just below the flight level where the data would most likely not be used anyway. In general, the accuracy is sufficient to make the technique promising for use in NWP. The vertical resolution of the observations based on the width of the first Fresnel zone is 200–240 m, which also makes the data source attractive for high-resolution studies of gravity waves and other small-scale vertical structures. Currently, the new HIAPER GISMOS RO system includes a GNSS recorder, which will enable open-loop tracking to mitigate the effects of atmospheric multipath in the GPS observations. However, additional development of more advanced retrieval methods for the airborne geometry must be developed in order to exploit these data, and will be the focus of future work.

Acknowledgment

The authors would like to thank S. Sokolovskiy of UCAR COSMIC for the assistance and advice. The authors would also like to thank two anonymous reviewers for their comments and for their encouragement to include an expanded treatment of the range of error sources. The Generic Mapping Tools (GMT) package was used to produce some of the figures in this paper.

References

[1] G. Fjeldbo, A. J. Kliore, and V. R. Eshleman, "The neutral atmosphere of Venus as studied with the Mariner V radio occultation experiments," *Astron. J.*, vol. 76, no. 2, pp. 123–140, Mar. 1971.

[2] E. R. Kursinski, G. A. Hajj, W. I. Bertiger, S. S. Leroy, T. K. Meehan, L. J. Romans, J. T. Schofield, D. J. McCleese, W. G. Melbourne, C. L. Thornton, T. P. Yunck, J. R. Eyre, and R. N. Nagatani, "Initial results of radio occultation observations of Earth's atmosphere using the Global Positioning System," *Science*, vol. 271, no. 5252, pp. 1107–1110, Feb. 1996.

[3] C. Rocken, R. Anthes, M. Exner, D. Hunt, S. Sokolovskiy, R. Ware, M. Gorbunov, W. Schreiner, D. Feng, B. Herman, Y.-H. Kuo, and X. Zou, "Analysis and validation of GPS/MET data in the neutral atmosphere," *J. Geophys. Res.*, vol. 102, no. D25, pp. 29 849–29 866, 1997.

[4] J. Wickert, T. Schmidt, G. Beyerle, R. Konig, and C. Reigber, "The radio occultation experiment aboard CHAMP: Operational data analysis and validation of vertical atmospheric profiles," *J. Meteorol. Soc. Jpn.*, vol. 82, no. 1B, pp. 381–395, Mar. 2004.

[5] G. A. Hajj, C. O. Ao, B. A. Iijima, D. Kuang, E. R. Kursinski, A. J. Mannucci, T. K. Meehan, L. J. Romans, M. D. Juarez, and T. P. Yunck, "CHAMP and SAC-C atmospheric occultation results and intercomparisons," *J. Geophys. Res.—Atmospheres*, vol. 109, no. D6, p. D06 109, Mar. 2004.

[6] Y.-A. Liou, A. G. Pavelyev, S.-F. Liu, A. A. Pavelyev, N. Yen, C.-Y. Huang, and C.-J. Fong, "FORMOSAT-3/COSMIC GPS radio occultation mission: Preliminary results," *IEEE Trans. Geosci. Remote Sens.*, vol. 45, no. 11, pp. 3813–3826, Nov. 2007.

[7] W. Schreiner, C. Rocken, S. Sokolovskiy, S. Syndergaard, and D. Hunt, "Estimates of the precision of GPS radio occultations from the COSMIC/FORMOSAT-3 mission," *Geophys. Res. Lett.*, vol. 34, no. 4, p. L04 808, Feb. 2007. DOI: 10.1029/2006GL027557.

[8] B. H. Wu, V. Chu, P. Chen, and T. Ting, "FORMOSAT-3/COSMIC science mission update," *GPS Solut.*, vol. 9, no. 2, pp. 111–121, Jul. 2005.

[9] X. Zou, H. Liu, R. A. Anthes, H. Shao, J. C. Chang, and Y. J. Zhu, "Impact of CHAMP radio occultation observations on global analysis and forecasts in the absence of AMSU radiance data," *J. Meteorol. Soc. Jpn.*, vol. 82, no. 1B, pp. 533–549, Mar. 2004.

[10] L. Cucurull, Y. H. Kuo, D. Barker, and S. R. H. Rizvi, "Assessing the impact of simulated COSMIC GPS radio occultation data on weather analysis over the Antarctic: A case study," *Mon. Weather Rev.*, vol. 134, no. 11, pp. 3283–3296, Nov. 2006.

[11] S. B. Healy and J. N. Thepaut, "Assimilation experiments with CHAMP GPS radio occultation measurements," *Q. J. R. Meteorol. Soc.*, vol. 132, no. 615, pp. 605–623, Jan. 2006.

[12] C. Zuffada, G. Hajj, and E. R. Kursinski, "A novel approach to atmospheric profiling with a mountain-based or airborne GPS receiver," *J. Geophys. Res.*, vol. 104, no. D20, pp. 24 435–24 447, 1999.

[13] S. B. Healy, J. Haase, and O. Lesne, "Abel transform inversion of radio occultation measurements made with a receiver inside the Earth's atmosphere," *Ann. Geophys.*, vol. 20, no. 8, pp. 1253–1256, Aug. 2002.

[14] O. Lesne, J. Haase, G. Kirchengast, J. Ramsauer, and W. Poetzi, "Sensitivity analysis for airborne sounding of the troposphere by GNSS radio occultation," *Phys. Chem. Earth*, vol. 27, no. 4/5, pp. 291–299, May 2002.

[15] A. Mousa and T. Tsuda, "Inversion algorithms for GPS downward looking occultation data: Simulation analysis," *J. Meteorol. Soc. Jpn.*, vol. 82, no. 1B, pp. 427–432, Mar. 2004.

[16] Y. Aoyama, Y. Shoji, A. Mousa, T. Tsuda, and H. Nakamura, "Temperature and water vapor profiles derived from downward-looking GPS occultation data," *J. Meteorol. Soc. Jpn.*, vol. 82, no. 1B, pp. 433–440, Mar. 2004.

[17] S. Danno, "Observation of refractive index profiles with GPS radio occultation from an airplane," M.S. thesis, Dept. Commun. Comput. Eng., Graduate School Informatics, Kyoto Univ., Kyoto, Japan, 2006.

[18] T. Yoshihara, N. Fujii, K. Hoshinoo, K. Matsunaga, S. Saitoh, T. Tsuda, Y. Aoyama, and S. Danno, "Airborne GPS downward-looking occultation experiment in 2003," presented at the Asia Oceania Geosciences Society, Singapore, 2004, Paper 57-IWG-A1831.

[19] K. K. Laursen, D. P. Jorgensen, G. P. Brasseur, S. L. Ustin, and J. R. Huning, "HIAPER: The next generation NSF/NCAR research aircraft," *Bull. Amer. Meteorol. Soc.*, vol. 87, no. 7, pp. 896–909, Jul. 2006.

[20] J. L. Garrison, M. Walker, J. S. Haase, T. Lulich, F. Xie, B. D. Ventre, M. H. Boehme, B. Wilmhoff, and S. J. Katzberg, "Development and testing of the GISMOS instrument," in *Proc. IGARSS*, Jul. 2007, pp. 5105–5108.

[21] E. R. Kursinski, G. A. Hajj, K. R. Hardy, J. T. Schofield, and R. Linfield, "Observing Earth's atmosphere with radio occultation measurements using the Global Positioning System," *J. Geophys. Res.—Atmospheres*, vol. 102, no. D19, pp. 23 429–23 465, Oct. 1997.

[22] W. G. Melbourne, E. S. Davis, C. B. Duncan, G. A. Hajj, K. R. Hardy, E. R. Kursinski, T. K. Meehan, L. E. Young, and T. P. Yunck, *The Application of Spaceborne GPS to Atmospheric Limb Sounding and Global Change Monitoring*. Pasadena, CA: Jet Propulsion Lab. JPL Publication 94-18, 1994.

[23] V. V. Vorobev and T. G. Krasil'nikova, "Estimation of the accuracy of the atmospheric refractive index recovery from Doppler shift measurements at frequencies used in the NAVSTAR system," *Phys. Atmos. Ocean (English Translation)*, vol. 29, no. 5, pp. 602–609, 1994.
[24] Y. H. Kuo, T. K. Wee, S. Sokolovskiy, C. Rocken, W. Schreiner, D. Hunt, and R. A. Anthes, "Inversion and error estimation of GPS radio occultation data," *J. Meteorol. Soc. Jpn.*, vol. 82, no. 1B, pp. 507–531, Mar. 2004.
[25] M. Born and E. Wolf, *Principles of Optics: Electromagnetic Theory of Propagation, Interference and Diffraction of Light*. New York: Pergamon, 1964.
[26] E. K. Smith and S. Weintraub, "The constants in the equation for atmospheric refractive index at radio frequencies," *Proc. IRE*, vol. 41, no. 8, pp. 1035–1037, Aug. 1953.
[27] P. Poli, J. Joiner, and E. R. Kursinski, "1DVAR analysis of temperature and humidity using GPS radio occultation refractivity data," *J. Geophys. Res.*, vol. 107, no. D20, p. A04 448, 2002. DOI: 10.1029/2001JD000935.
[28] A. K. Steiner, G. Kirchengast, and H. P. Ladreiter, "Inversion, error analysis, and validation of GPS/MET occultation data," *Ann. Geophys.*, vol. 17, no. 1, pp. 122–138, Jan. 1999.
[29] GRAS-SAG, *Report of the GRAS-SAG: The GRAS instrument on METOP*. EUMETSAT 5, Jan. 1998.
[30] P. Hoeg, A. Hauchecorne, G. Kirchengast, S. Syndergaard, B. Belloul, R. Leitinger, and W. Rothleitner, "Derivation of atmospheric properties using a radio occultation technique," Danish Meteorol. Inst., Copenhagen, Denmark, ESA Contract Rep. (ESTEC/C. No. 11024/94/NL/CN) DMI Scientific Rep. 95-4, 1995.
[31] S. B. Healy, "GPS radio occultation assimilation at ECMWF," in *Proc. 2nd FORMOSAT-3/COSMIC* Data *Users Workshop*, Boulder, CO, 2007.
[32] J. Wang, D. J. Carlson, D. B. Parsons, T. F. Hock, D. Lauritsen, H. L. Cole, K. Beierle, and E. Chamberlain, "Performance of operational radiosonde humidity sensors in direct comparison with a chilled mirror dew-point hygrometer and its climate implication," *Geophys. Res. Lett.*, vol. 30, no. 16, p. 1860, Aug. 2003. DOI: 10.1029/2003GL016985.
[33] G. Beyerle, T. Schmidt, J. Wickert, S. Heise, M. Rothacher, G. Konig-Langlo, and K. B. Lauritsen, "Observations and simulations of receiver-induced refractivity biases in GPS radio occultation," *J. Geophys. Res.*, vol. 111, no. D12, p. D12 101, Jun. 2006. DOI: 10.1029/2005JD006673.
[34] S. Sokolovskiy, Y. H. Kuo, C. Rocken, W. S. Schreiner, D. Hunt, and R. A. Anthes, "Monitoring the atmospheric boundary layer by GPS radio occultation signals recorded in the open-loop mode," *Geophys. Res. Lett.*, vol. 33, no. 12, p. L12 813, Jun. 2006. DOI: 10.1029/2006GL025955.
[35] J. Nash, R. Smout, T. Oakley, B. Pathack, and S. Kurnosenko, "WMO intercomparison of radiosonde systems," World Meteorol. Org., Geneva, Switzerland, Instruments and Observing Methods Rep. No. 83, WMO/TD-No. 1303, 2006.
[36] B. Herman, E. R. Kursinski, D. Feng, D. Flittner, D. Ward, S. Syndergaard, and E. M. Lane, "Active tropospheric ozone and moisture sounder (ATOMS)," Univ. Arizona, Tucson, AZ, Science Rep. NASA Contract NAS1-99055, 2003.
[37] S. Syndergaard, E. R. Kursinski, B. M. Herman, E. M. Lane, and D. E. Flittner, "A refractive index mapping operator for assimilation of occultation data," *Mon. Weather Rev.*, vol. 133, no. 9, pp. 2650–2668, Sep. 2005.
[38] J. R. Eyre, "Assimilation of radio occultation measurements into a numerical prediction system," Eur. Centre Medium-Range Weather Forecasts, Reading, U.K., Tech. Memo. 199, 1994.
[39] M. E. Gorbunov, K. B. Lauritsen, A. Rhodin, M. Tomassini, and L. Kornblueh, "Radio holographic filtering, error estimation, and quality control of radio occultation data," *J. Geophys. Res.*, vol. 111, no. D10, p. D10 105, May 2006. DOI: 10.1029/2005JD006427.
[40] M. D. Mortensen and P. Hoeg, "Inversion of GPS occultation measurements using Fresnel diffraction theory," *Geophys. Res. Lett.*, vol. 25, no. 13, pp. 2441–2444, Jul. 1998.
[41] S. Sokolovskiy, "Modeling and inverting radio occultation signals in the moist troposphere," *Radio Sci.*, vol. 36, no. 3, pp. 441–458, 2001.
[42] J. L. Garrison, B. D. Ventre, J. S. Haase, and M. H. Boehme, "Development and testing of the GNSS instrument system for multistatic and occultation sensing (GISMOS) airborne instrument," in *Proc. Amer. Geophys. Union Fall Meeting*, San Francisco, CA, 2006.
[43] F. Xie, S. Syndergaard, E. R. Kursinski, and B. M. Herman, "An approach for retrieving marine boundary layer refractivity from GPS occultation data in the presence of superrefraction," *J. Atmos. Ocean. Technol.*, vol. 23, no. 12, pp. 1629–1644, Dec. 2006.
[44] S. Han and C. Rizos, "Airborne GPS kinematic positioning and its application to oceanographic mapping," *Earth Planets Space*, vol. 52, no. 10, pp. 819–824, 2000.
[45] Q. J. Zhang and K. P. Schwarz, "Estimating double difference GPS multipath under kinematic conditions," in *Proc. IEEE Position Location Navigat. Symp.*, pp. 285–291, 1996.
[46] R. Stolz, A. Lipp, B. Tiemeyer, and C. Discher, "Investigation of multipath effects in the vicinity of an aircraft dependent on different flight profiles," EUROCONTROL, Brétigny-sur-Orge, France, EEC Rep. 357, Dec. 2000.
[47] J. Wickert, G. Beyerle, G. A. Hajj, V. Schwieger, and C. Reigber, "GPS radio occultation with CHAMP: Atmospheric profiling utilizing the space-based single difference technique," *Geophys. Res. Lett.*, vol. 29, no. 8, p. 1187, Apr. 2002. DOI: 10.1029/2001GL013982.

Feiqin Xie received the B.S. degree in atmospheric sciences from Lanzhou University, Lanzhou, China, in 1998, the M.S. degree from Peking University, Beijing, China, in 2001, and the Ph.D. degree from the University of Arizona, Tucson, in 2006.

He is currently with the Jet Propulsion Laboratory, Pasadena, CA. He was previously a Postdoctoral Research Scholar with the Department of Earth and Atmospheric Sciences, Purdue University, West Lafayette, IN. His primary research objective includes atmospheric remote sensing using spaceborne and airborne GPS radio occultation technique and planetary boundary layer dynamics.

Jennifer S. Haase received the B.S. degree in geophysics from the California Institute of Technology, Pasadena, in 1985 and the Ph.D. degree in earth science from the Scripps Institute of Oceanography, La Jolla, CA, in 1992.

From 1993 to 1995, she was a Research Fellow with the California Institute of Technology, specializing in seismology. From 1996 to 2001, she was a Research Scientist with ACRI, S.A., France, developing methods for studying the atmosphere with GPS signals. She is currently an Assistant Professor with the Department of Earth and Atmospheric Sciences, Purdue University, West Lafayette, IN. Her current fields of interest include atmospheric remote sensing and seismology.

Dr. Haase is a member of the American Geophysical Union, American Meteorological Society, and the Seismological Society of America.

Stig Syndergaard received the B.S. and M.S. degrees in geophysics and the Ph.D. degree in natural sciences from the University of Copenhagen, Copenhagen, Denmark, in 1990, 1995, and 1999, respectively.

From 2000 to 2007, he was a Research Associate and Research Scientist with the University of Arizona, Tucson, and a Visiting Scientist with the COSMIC Project Office, University Corporation for Atmospheric Research, Boulder, CO. He is currently a Scientist with the Danish Meteorological Institute, Copenhagen, where he primarily works with the processing, validation, and analysis of radio occultation data from the European MetOp satellite.